Carbon 95 (2015) 738–745

Contents lists available at ScienceDirect

Carbon

journal homepage: www.elsevier.com/locate/carbon

Electron-beam writing of deoxygenated micro-patterns on graphene oxide film

Kuang-Hsu Wu [a, 1], Han-Hao Cheng [b, 1], Ali Amdad Mohammad [a], Idriss Blakey [b], Kevin Jack [c], Ian R. Gentle [a], Da-Wei Wang [a, d, *]

[a] School of Chemistry and Molecular Biosciences, The University of Queensland, Brisbane, QLD 4072, Australia
[b] Australian Institute for Bioengineering and Nanotechnology, The University of Queensland, Brisbane, QLD 4072, Australia
[c] Centre for Microscopy and Microanalysis, The University of Queensland, Brisbane, QLD 4072, Australia
[d] School of Chemical Engineering, The University of New South Wales, Sydney, NSW 2052, Australia

ARTICLE INFO

Article history:
Received 22 July 2015
Received in revised form
29 August 2015
Accepted 31 August 2015
Available online 3 September 2015

ABSTRACT

Electron-beam (e-beam) lithography at a low energy can efficiently write deoxygenated micro-patterns on graphene oxide (GO) films with high edge-definition. The deoxygenation caused by the secondary process of back-scattered electrons leads to a shrinkage of pattern height. A lower energy e-beam is found to be more effective in deoxygenating of GO than that by using a higher energy e-beam. The thickness and the oxygen-to-carbon atomic ratio of the pattern are strongly related that decreases progressively with increasing the electron dosage before reaching a steady level. In addition, as the electron dose increases the patterned area also expanded in lateral direction. The observations of the proximity effect are justified with our results and the Monte Carlo simulation of electrons trajectories. These results can be a guideline for the fabrication of all-carbon thin film electronics.

1. Introduction

The emerging research towards graphene-based micro-electronics originates from the unique electronic, thermal and mechanical properties of the single layer carbon sheet [1,2]. In particular, graphene-based materials have attracted much attention of electronics industries owing to their great versatility by opening up the band gap through introduction of physical constraints (lateral size and defect) or chemical modifications (doping and functionalization) [3–7]. By this advantage, graphene derivatives have shown their applications as various important electronic components, such as field-effect transistors, diodes, supercapacitors, electronic circuits, memory cells and circuit substrates [8–16]. The wide application of semiconducting graphene derivatives has therefore brought up the idea of printable all-carbon micro-electronics on flexible substrates [15–19]. However, one major difficulty of the idea is the creation of miniaturized electronic components at desired substrate locations. Typically, this requires sophisticated lithographic processes to locate target materials and to remove auxiliary masks. When graphene oxide (GO) is the substrate, the process can be much simplified by reductive lithographic patterning on the substrate to create conductive paths or semiconducting patterns, depending on the degree of deoxygenation [20–23]. For example, direct inkjet printing of conductive circuits and laser-beam writing of deoxygenated patterns on a GO film can efficiently produce millimeter-scale graphene-based electronic components [10–12]. Unfortunately, these techniques are typically incompetent for micro-electronics fabrication, owing to the large spot size of the print-head and the laser-beam.

As an alternative, electron-beam lithography (EBL) offers highly focused beam line and can render nanometer-to micrometer-scale patterns on a soft substrate [24]. Moreover, electron-beam (e-beam) irradiation has demonstrated the ability of reducing GO to create locally deoxygenated micro-patterns on a GO substrate using moderate to high energy e-beams [25–27]. However, high-energy e-beams often provide low throughput and can cause substrate damage and strong proximity effect on polymer resists [28–30]. In this report, we have demonstrated the use of low-energy e-beam to write edge-defined micro-patterns on a GO film. Atomic force microscopy (AFM), scanning electron microscopy (SEM) and optical microscopy revealed the morphology and the visible features of the

* Corresponding author. School of Chemical Engineering, The University of New South Wales, Sydney, NSW 2052, Australia.
E-mail address: da-wei.wang@unsw.edu.au (D.-W. Wang).
[1] These authors contributed equally.

http://dx.doi.org/10.1016/j.carbon.2015.08.116
0008-6223/

micro-patterns. X-ray photoelectron spectroscopy (XPS), energy dispersive spectroscopy (EDS) and Raman spectroscopy suggested that the low-energy e-beam deoxygenates the surface of patterned area without restoring or further damaging the lattice structure of GO. The effect of electron dose on pattern properties was further investigated and correlated with the results obtained from Monte Carlo simulations.

2. Experimental section

2.1. Synthesis of the graphene oxide

A modified Hummer's method was employed to prepare GO from expandable graphite flakes (GrafGuard 160-50-N, Graftech, USA) [31]. Basically, 120 mL of concentrated H_2SO_4 was added to a mixture of graphite (1.0 g) and $KMnO_4$ (6.0 g). The reaction flask was quickly transferred into a 50 °C bath for continuous stirring over 4 h. After cooling the reaction mixture to room temperature, 3 mL 30 vol.% H_2O_2 together with 100 mL water was poured into it. The mixture was centrifuged (4500 rpm for 30 min), and the supernatant decanted away. The product gel was washed and centrifuged repeatedly for at least 5 times using deionized water until the pH of the supernatant was close to 7. The gel was re-dispersed in water (1 mg/mL), subjected to probe ultrasonication, resulting in a stable colloidal GO solution.

2.2. Electron-beam writing of deoxygenated GO pattern

A GO film substrate was prepared as follows: 6 μL of the GO suspension was drop-cast and dried on a clean, polished Si wafer to form a thin GO film; the film thickness was determined to be 220 nm, using a stylus surface profiler (Dektek 150). Inside the vacuum chamber of a JEOL 6610 scanning electron microscope, the raw GO film was irradiated with an e-beam at a beam current of 2.0 nA to create a 3 × 3 array of 20 μm × 20 μm square micro-patterns at different given electron dose, from 5 mC cm^{-2} to 500 mC cm^{-2}. The movement of the e-beam was programmed by a Raith EBL system. Both 5 kV and 20 kV e-beams were used to pattern the square array at the same condition for direct comparison.

2.3. Characterization of the GO films

AFM was performed by using a MFP-3D (Asylum Research) atomic force microscope in ambient air. The microscope is mounted on an anti-vibrational table (Herzan) and operated within an acoustic isolation enclosure (TMC, USA). The cantilevers used in this study were conductive (Pt coated) NSG03 model, from NT-MDT (Russia), having a nominal resonant frequency between 50 kHz and 150 kHz. SEM was performed on a JEOL 6610 scanning electron microscope at 15 kV, equipped with an Oxford EDS detector for EDS measurement. For the EDS measurements on the square micro-patterns, at least 5 samples were collected and the errors were based on the standard deviation. Optical microscopy was carried out on an optical microscope (Olympus BX61). Image analysis and color inversion were performed using ImageJ 1.48v to promote visual effect and analysis; the transforming parameters were kept constant to ensure minimal alteration to the raw data. XPS was recorded using a Kratos Axis Ultra spectrometer with Al Kα radiation (15 kV, 150 W). The XPS survey was collected over 0 eV–1200 eV with pass energy of 160 eV and an energy interval of 1 eV/step. The high resolution XPS spectra were measured with a width of 14–20 eV, pass energy of 20 eV and an energy interval of 0.05 eV/step.

2.4. Monte Carlo simulation of electron trajectories

The Monte Carlo simulation of electron trajectories was performed on CASINO v2.42 software package. A two-layer model similar to our experimental condition was employed for the simulation: a layer comprised of carbon and oxygen at a ratio of 70:30 with a thickness of 220 nm and a layer of pure Si substrate with infinite thickness. The simulated number of electrons for each condition was 200,000 and the beam voltages varied from 5 kV to 20 kV.

3. Results and discussion

Fig. 1a depicts a schematic diagram of the EBL process. A GO film was formed by drop-casting on a polished silicon wafer, and the e-beam writing using an EBL system was directly performed on a relatively flat area of the film to create square micro-pattern arrays (an optical image of the drop-cast GO film with micro-pattern arrays can be found in Fig. S1, Supporting information). The morphology of the micro-patterns was characterized by AFM. In Fig. 1b, the patterned squares were shrunken in height after electron-beam irradiation, as shown by the dark purple area. The thickness reduction is a typical characteristic of GO reduction through removal of the intercalate water molecules and oxygen groups that support the puffy GO stacking. Wei et al. as well observed a decrease in the film thickness when they used a hot AFM tip to reduce a GO film [32]. Moreover, the extent of shrinkage is associated with the amount of given electron dose. Fig. 1c shows the surface profile along the path of the black arrow in the AFM micrograph; the grey arrow in the figures indicates the interference from contaminant particulate matter. The result suggests that the e-beam irradiation indeed decreased the thicknesses of the irradiated areas by ~78 and ~65 nm for the irradiation of 100 and 50 mC cm^{-2} electron dose, respectively. We also evaluated the sample heights for the micro-patterns at higher electron dosages. Fig. S2, Supporting information shows that the reduced sample height is dependent on the electron dosage in a saturating growth behavior. In general, a higher electron dose can give rise to a greater degree of deoxygenation and therefore result in a stronger shrinkage in the sample height.

As it was seen that the decrease in thickness is related to the electron dose, we therefore investigated the effects of electron dose on the patternability. Fig. 2a and b displays the SEM and optical images of (3 × 3) arrays of square micro-patterns. Each pattern was given by a certain electron dose using e-beams at two different accelerating voltages (5 kV and 20 kV). A gradual change in gray-scale contrast of the square patterns in the SEM and optical micrographs can be observed along with increasing electron dose for both 5 kV and 20 kV patterns. This probably suggests that the micro-patterns at high doses are relatively more deoxygenated. For the patterns produced by a 5 kV e-beam, there shows distinct square patterns with excellent edge-definition for all the electron doses. In contrast, the micro-patterns produced by a 20 kV e-beam appear to be murky at low electron doses (5–20 mC cm^{-2}) and the high-dose patterns exhibit diffuse edges that make the square patterns appear to be slightly bigger than their expected sizes. Clearly, the proximity effect is much stronger in the patterning using a higher energy e-beam.

In an effort to quantify the proximity effect by e-beams at different energies, we inverted the color of the optical micrographs to enhance the contrast of pattern edges for the purpose of image analysis. Fig. 2c displays the color-inverted optical micrographs; the target patterning area and the observed pattern area are respectively framed by yellow and pink boxes. The 5 kV beam-scribed patterns demonstrated very little proximity effect given by their

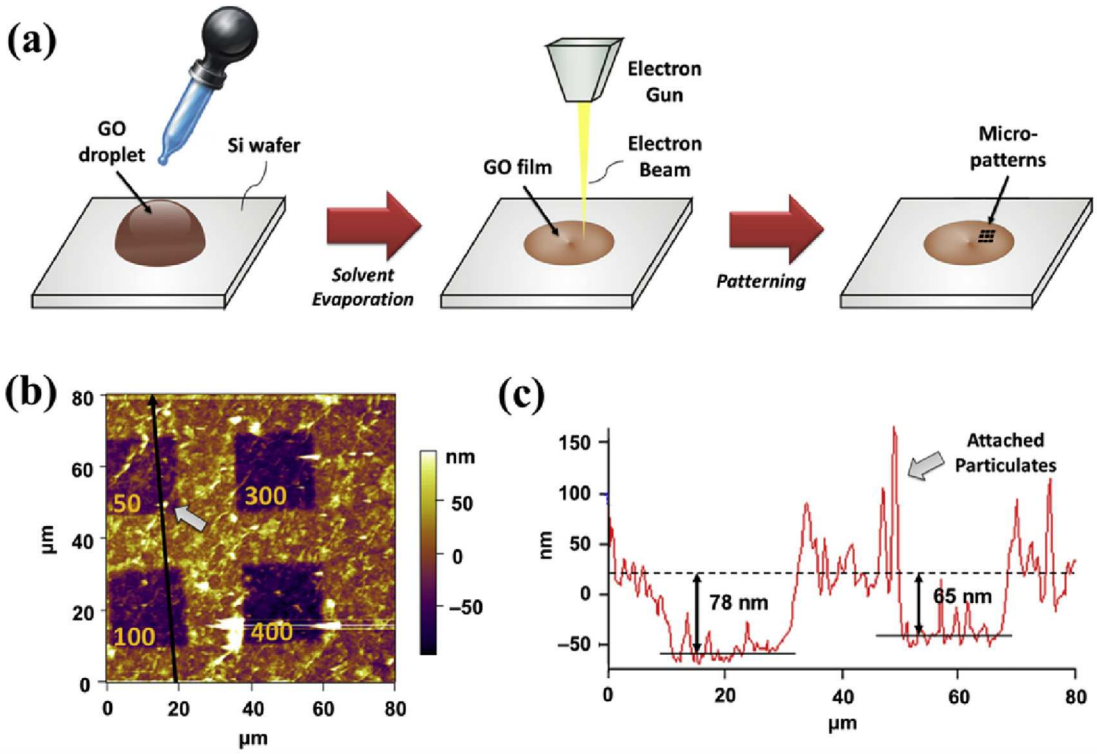

Fig. 1. (a) Schematic diagram of the e-beam patterning process on a drop-cast GO film. (b) AFM topographic image of the square micro-patterns; number indicates electron dosage (mC cm^{-2}). (c) Surface profile across the square micro-patterns (along the path of the black arrow in the AFM image) scribed with a 5 kV e-beam. (A colour version of this figure can be viewed online.)

small size expansion (0.60 ± 0.09 μm extension from one side @ 500 mC cm^{-2}), whereas such effect was much stronger in the squares written by a 20 kV e-beam (3.05 ± 0.21 μm extension from one side @ 500 mC cm^{-2}). This proximity effect should be due to the large electron–matter interaction volume and the subsequent physical processes delivered by high-energy e-beam [28]. In a later discussion, we will address the mechanism of the proximity effect on GO with the help of Monte Carlo simulations of electron trajectories in the sample. Nevertheless, the results suggest that GO patterning using EBL can generate micro-patterns with a decent lithographic resolution when a low-energy e-beam is used.

We further evaluated the correlation between the optical color contrast and electron dose using different e-beam energies. Image analysis was again performed on the color-inverted optical micrographs to minimize background interference; the relative intensity of contrast should stay unchanged when the transforming parameters were kept the same. Despite of the dark-colored scheme, it can be picked up that the color of the square patterns turned from dark purple to black upon exposure to high electron doses. The optical contrast values of the micro-patterns in reference to the raw GO film without e-beam irradiation were plotted against the electron dose for the two sets of squares, as shown in Fig. 2d. The optical contrast for both cases displays a saturating growth behavior along with increasing electron dose. If the optical contrast values are directly associated with the degree of chemical change, then there is likely a progressive deoxygenation with an extended e-beam exposure time. Furthermore, the contrast values for the 5 kV patterns stay stably at a higher level than that for the 20 kV patterns over the range of electron dose. This means that the low-energy e-beam can perform reductive lithographic patterning of GO more effectively than the higher energy e-beam. This is in agreement with the results of EBL on polymer resists using low-energy e-beams [28,30]. Interestingly, the level of relative optical contrast is 1.5-fold higher for the 5 kV patterns than that for the 20 kV patterns for all of the electron doses. The constant relative contrast value within the examined range of electron dose suggests that the relative extent of GO reduction within the patterns is closely related to the relative beam accelerating voltage when the beam current is controlled, irrespective of the given electron dose. In a mathematical expression, the relationship may be described in Eq. (1), where θ is the optical contrast, V is the beam accelerating voltage and α is an auxiliary coefficient corresponding to each e-beam patterning process.

$$\frac{\theta_1}{\theta_2} = \frac{\alpha_2 V_2}{\alpha_1 V_1} \tag{1}$$

If we treat the relative optical contrast as a reflection of the relative amount of electrons "stored" in the GO patterns at each beam voltage, then Eq. (1) is equivalent to an expression of relative capacitance (Eq. (2), $C = q/V$), where β is the percentage gain of incident electrons by the patterns.

$$\frac{C_1}{C_2} = \frac{\beta_2 V_2}{\beta_1 V_1} \tag{2}$$

In this situation, the auxiliary coefficient, α in Eq. (1) is basically analogous to β, and the α_2/α_1 value would provide the relative efficiency of electron gain. For the present example, a α_2/α_1 value of 0.375 can be found by inserting the measured value of relative optical contrast and the beam voltages. This means that the electron gain by the square patterns created by a 20 kV e-beam is only 37.5% of that created by a 5 kV e-beam. Therefore, it is clear that the reductive patterning of a GO film is more energy efficient with a low-energy e-beam than with higher energy e-beams. Despite the observation of a constant relative contrast inside the examined range of electron dose, it is expected that the relative contrast

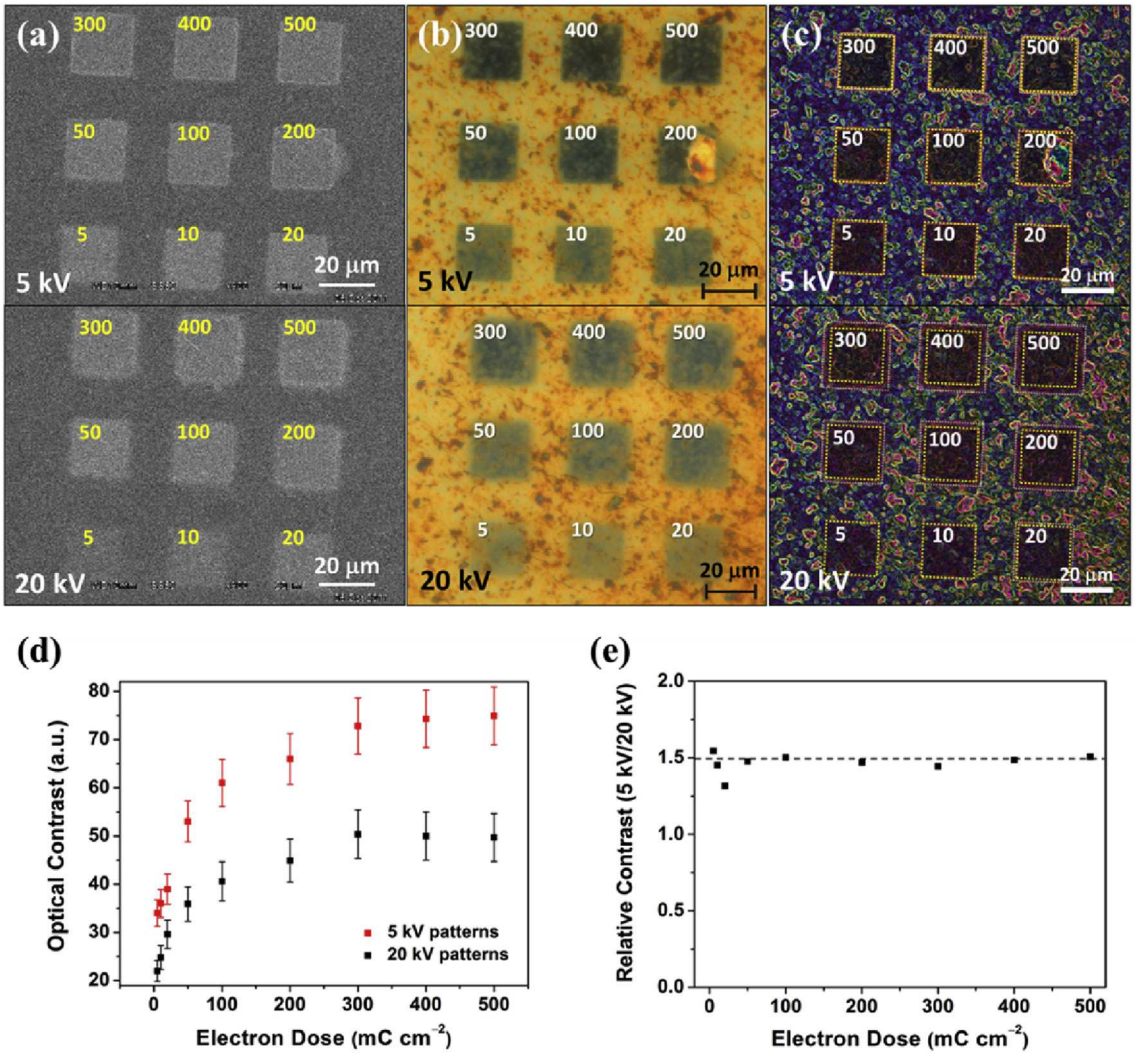

Fig. 2. (a) SEM and (b) optical micrographs of 3 × 3 arrays of square micro-patterns at different electron dose (mC cm^{-2}) using 5 kV (top) and 20 kV (bottom) e-beams; (c) the color-inverted optical micrographs for a better visual contrast of the pattern size. (d) A plot of optical contrast against electron dose for 5 kV and 20 kV micro-patterns and (e) the relative optical contrast of the patterns (5 kV/20 kV). (A colour version of this figure can be viewed online.)

would finally arrive at a value of 1.0 when the GO pattern reaches a saturated reduced state.

XPS and EDS are powerful micro-analytical techniques that allow surface and small-area composition analyses. Unfortunately these techniques cannot provide accurate composition of patterns that are both small and thin, due to the nature of their measurements. For instance, XPS can afford decent surface analysis (up to 10 nm into the sample), but the analytical area is approximately 100 μm, limited by the spot size of the laboratory X-ray beam. While EDS can offer small-area analysis by the small beam spot size, the energetic e-beam can penetrate deeply into the sample (typically ~2 μm into a carbonaceous sample for a 15 kV e-beam) and interact with the matter for a bulk-like analysis. In a purpose to recognize the chemical composition of raw GO film and the patterns, we firstly studied the composition of a large-area GO pattern (100 μm × 150 μm) at an initial (raw) state and at a highly reduced state after given a very high dose (>8000 mC cm^{-2}) using a 20 kV e-beam. The optical images of the raw and reduced pattern are displayed in Fig. 3a. Obviously the high-dose, irradiated pattern exhibited a very dark color as compared to the raw film. In Fig. 3b, the XPS survey spectra confirm that the irradiated pattern was greatly deoxygenated. Only oxygen and carbon signatures were found in the spectra and the oxygen-to-carbon (O/C) atomic ratio of the GO pattern has changed from 0.422 (raw) to a ratio of 0.213 (irradiated). This suggests that a considerable amount of oxygen has been removed from the pattern after the e-beam irradiation. Furthermore, we characterized the small square patterns (Fig. 2a–c) with EDS for a qualitative investigation. Fig. 3c is a sample EDS spectra collected at two different positions in a micro-pattern array (by a 20 kV e-beam). In agreement with the XPS result, the O/C ratio is much lower at inside of the square pattern than at the outside. This directly confirms that e-beam irradiation can induce deoxygenation (and reduction) of GO and lead to a gray-scale contrast under a SEM or a color contrast under an optical microscope. Moreover, we collected the EDS spectra of each square pattern given by 5 kV and 20 kV beam, and the O/C atomic ratios are displayed in Fig. 3d. Since EDS could only provide a bulk-like analysis, the measured composition is an average of the reduced pattern and the unmodified GO beneath it. Nonetheless, the result still reflects the trend of progressive deoxygenation of the patterns along the given electron dose. A similar decreasing behavior in the O/C ratio was observed for both the 5 kV and 20 kV patterns. It is worthy to note that the O/C ratio maintained at a lower level for the 5 kV patterns than for the 20 kV patterns. Even at a very low dose

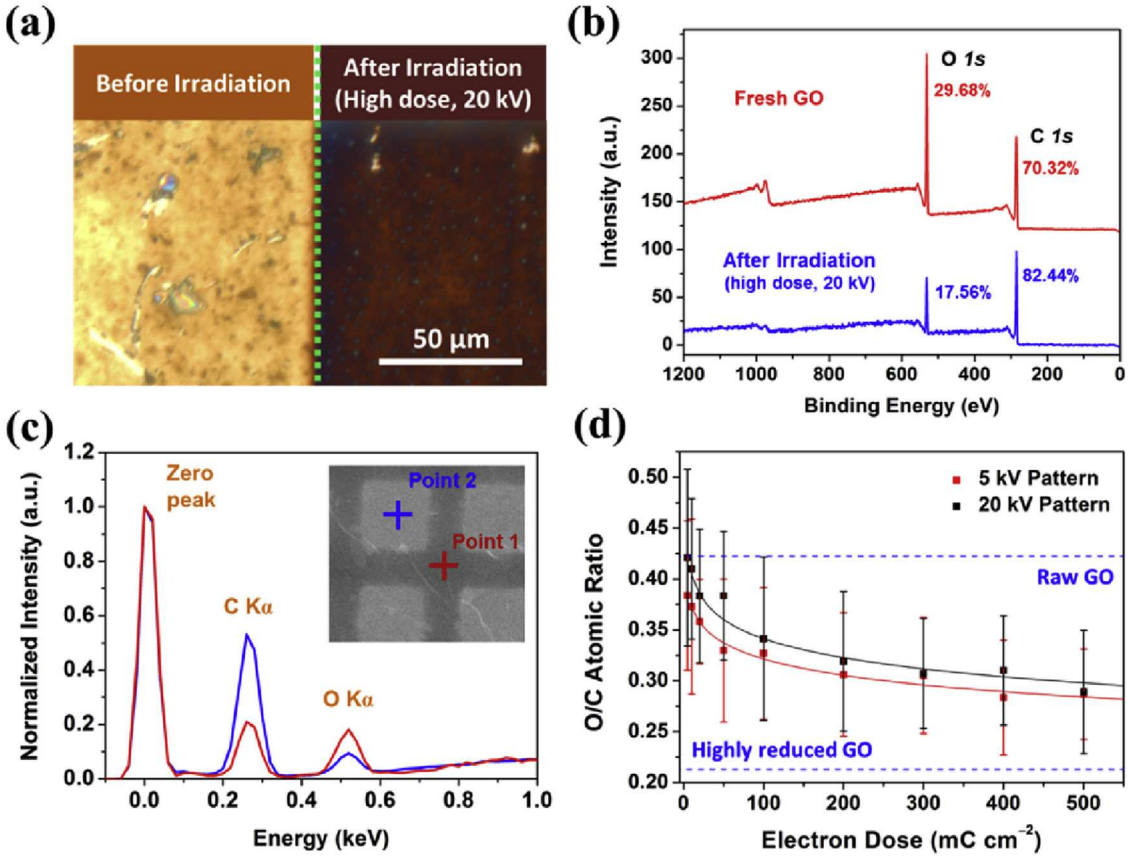

Fig. 3. (a) Optical micrographs of a large-area GO pattern before and after given a very high dose at 20 kV, and (b) the XPS survey spectra of the raw and irradiated patterns. (c) The EDS spectra at two positions in a micro-pattern array, and (d) the O/C atomic ratios of the square micro-patterns at different electron dose produced by 5 kV and 20 kV e-beams. (A colour version of this figure can be viewed online.)

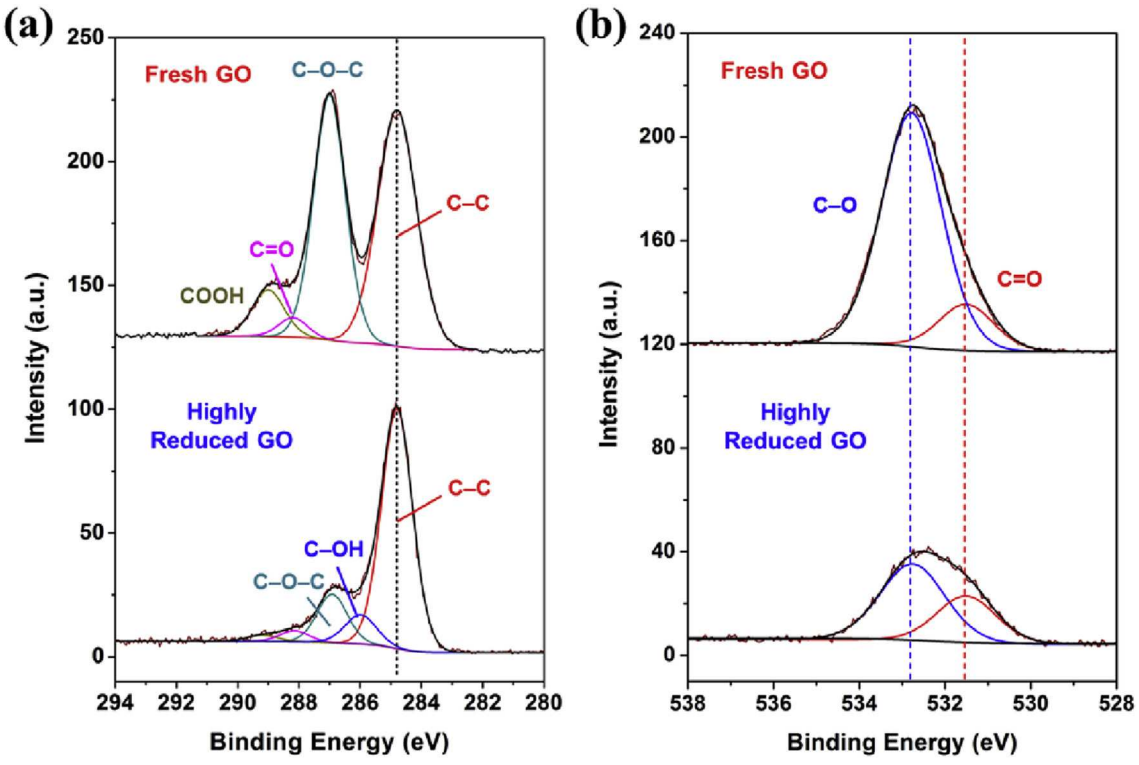

Fig. 4. High-resolution XPS (a) C *1s* and (b) O *1s* spectra of raw GO and highly reduced GO. (A colour version of this figure can be viewed online.)

($5\ mC\ cm^{-2}$), the pattern created by 5 kV beam could show obvious difference in the O/C ratio (O/C = 0.384) in reference to raw GO film (O/C = 0.422). In contrast, there is almost no change in the O/C ratio for the low-dose pattern created by 20 kV beam (O/C = 0.421). This result again suggests the better efficiency of using low-energy e-beam in the direct deoxygenation of GO film.

The chemistry of GO before and after e-beam irradiation was studied by high-resolution XPS. Fig. 4 shows the deconvoluted C *1s* spectra and O *1s* spectra of a large-area GO pattern before and after irradiation. Clearly, the raw GO film was rich in oxygen functional groups such as epoxide (C–O–C, 287.0 eV), carbonyl (C=O, 288.2 eV) and carboxyl (COOH, 289.0 eV) groups, as given in Fig. 4a. These are typical functional groups of GO, as reported in the literature [33,34]. After irradiation, the relative intensity of the oxygen-containing groups significantly decreased with a small amount of hydroxyl (C–OH, 286.0 eV) groups was produced. It is also interesting to note that the carbonyl/carboxyl groups were almost completely removed after the irradiation. In a typical thermal deoxygenation of GO, the epoxide groups could be largely removed at a temperature of 200 °C, whereas the carbonyl/carboxyl groups are only eradicated at above 400 °C [35]. Perhaps this suggests that e-beam irradiation is effective in getting rid of these oxygen groups. On the other side, the O *1s* spectra in Fig. 4b also support the significant removal of epoxide groups by e-beam irradiation. The large reduction of C–O (532.8 eV) relative to C=O (531.5 eV) means that there were much more epoxide groups removed than the carbonyl/carboxyl groups. From above, it is clear that e-beam irradiation on GO can remove a large amount of the epoxide group and almost eliminate the carbonyl/carboxyl groups.

Raman spectroscopy can provide information about structural disorder in the graphitic lattice of GO. Fig. 5 displays the Raman spectra of the GO film treated with different electron doses by 5 kV and 20 kV e-beams, respectively. There are two main peaks relating to the first-order phonon vibration of the carbon lattice: D ($1352\ cm^{-1}$, ring breathing mode) and G ($1605\ cm^{-1}$, stretching mode); the hump at ~$2800\ cm^{-1}$ (2D) is associated with the second-order overtone of the D band [36]. The D and G bands are very similar in the peak features, and the spectral envelope of the patterns can be superimposed with each other. This result suggests that the e-beam irradiation does not restore the structural disorder or incur further damage in GO during the deoxygenation process. It is to be noted that a considerable amount of fluorescence, which is attributable to the oxygen-containing groups (C–O, C=O and COOH) nearby the remaining sp^2 carbon domains [37], was observed in a raw GO film (Fig. S3, Supporting information) and the intensity of the fluorescence sharply dropped with the introduction of e-beam irradiation. Most of the fluorescence dropped in the 5 kV patterns after irradiation with a dose of $5\ mC\ cm^{-2}$, while a small extent of the fluorescence intensity remained in the 20 kV sample. This small quantity of the fluorescence diminished with increasing electron dose. This observation suggests that the 5 kV patterns were effectively deoxygenated to an extent that could significantly quench the fluorescence.

To elucidate the reason behind the strong proximity effect and the poor deoxygenation capability when using higher energy e-beams, we performed a Monte Carlo simulation of electron trajectory using different beam energies on CASINO v2.42 [38]. For the proximity effect, we evaluated the surface distribution radius of back-scattered electrons (BSEs) for beam voltages at 5 kV and 20 kV (surface distribution radii at different voltages are shown in Fig. S4, Supporting information). The surface distribution of BSEs basically tells about the population of projected BSEs at each position on the sample surface. Fig. 6a shows the surface distribution radius of BSEs on a model GO film with a composition of $C_{70}O_{30}$ at the two beam voltages. Obviously the surface distribution of BSEs of a 5 kV beam

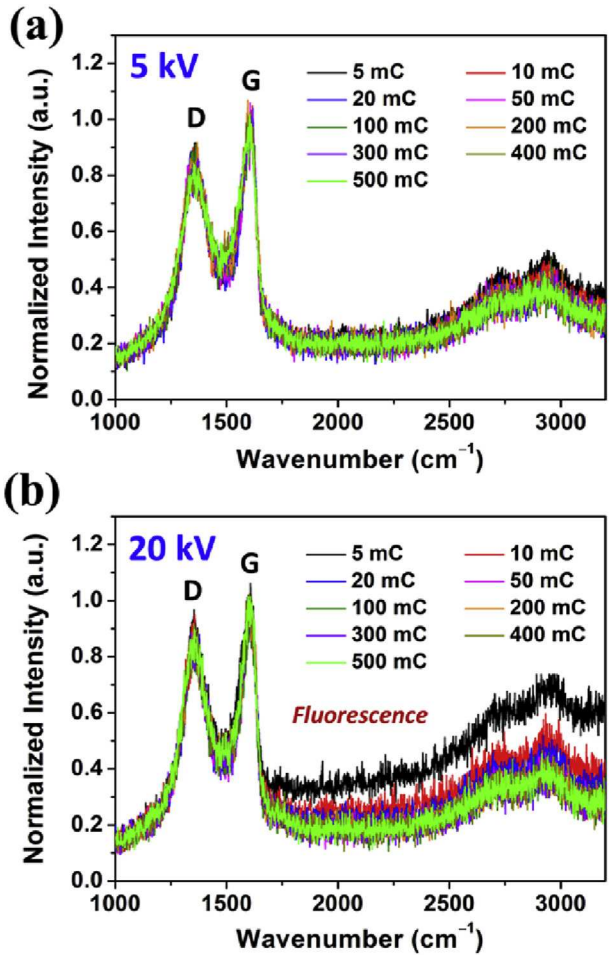

Fig. 5. Raman spectra of the square micro-patterns at different electron dosage by using (a) 5 kV and (b) 20 kV e-beams; the dosages are in units per cm^2. (A colour version of this figure can be viewed online.)

(radius = 0.36 μm) is much narrower than that of a 20 kV beam (radius = 3.40 μm). Interestingly, these values are fairly similar to the measured extended length of the square patterns (0.60 ± 0.09 μm and 3.05 ± 0.21 μm for 5 kV and 20 kV, respectively, at $500\ mC\ cm^{-2}$). This suggests that the effective patterning area must be closely related to the surface distribution of BSEs rather than to the incident electron (where there should be no size expansion of the pattern). Despite this, BSEs are perhaps not the direct source of electrons for the reductive patterning because BSEs typically have a slightly lower energy than the incident primary e-beam. From the comparative study of patterning efficiency, it is clear that the highly penetrative incident electrons do not effectively reduce the GO unless they are at a much lower energy. In this situation, low-energy secondary electrons that come from the electron–matter interaction (with mainly BSEs and primary electrons) are the more likely sources of reducing electrons. Since the secondary electrons (the mean-free-path is at an nm scale) are generated along the trajectory of energetic back-scattered electrons, the probable locations where the BSEs pass through would become reduced.

We further investigated the penetrating ability of incident primary electrons at different beam accelerating voltages, as shown in Fig. 6b. The electrons at a higher energy clearly tend to penetrate deeper into the sample and possibly further into the substrate without being absorbed. For a given amount of electrons, a crowd of energetic electrons has much greater probability to escape from the

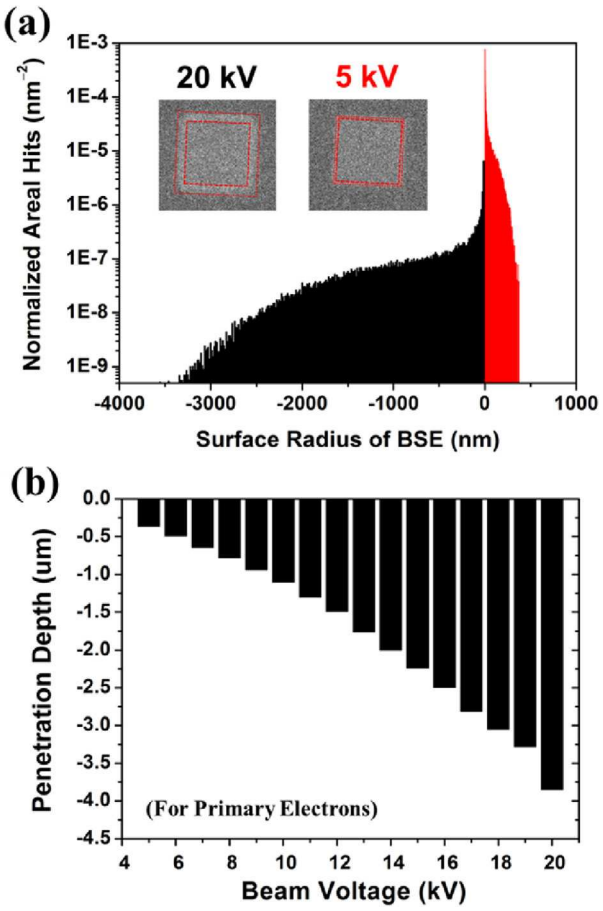

Fig. 6. (a) Simulated surface distribution radius of BSEs for a GO film with an atomic composition of $C_{70}O_{30}$ and a thickness of 220 nm at 5 kV and 20 kV beam accelerating voltages; the insets are the square (20 μm × 20 μm) patterns at an electron dose of 500 mC cm^{-2} at the two accelerating voltages. (b) The penetration depth of primary electrons from incident beam at different accelerating voltages. (A colour version of this figure can be viewed online.)

sample (our GO film thickness is 220 nm, while electrons can travel down to 4 μm from the sample surface with a 20 kV e-beam) than low-energy electrons. The penetration depth for the 5 kV e-beam is about 350 nm which is much less than that for 20 kV e-beam and comparable with the GO film thickness. It is probable that a higher portion of 5 keV primary electrons are back-scattered to the GO film generating extra amount of secondary electrons compared with the 20 keV primary electrons. With less probability of escaping, these low-energy secondary electrons, either from primary electrons during penetration or from BSEs, are capable of providing an efficient and effective reductive patterning of GO, while with excellent edge-definition and thus lithographic resolution.

Altogether, the proximity effect may be explained by a schematic diagram as shown in Fig. 7. As the incident e-beam hits the sample, the energetic electrons spread into the material and create an electron–matter interaction volume (V_i) in a drop-like shape; the size of V_i depends on the beam voltage. Most of the energetic electrons penetrate through the film to the substrate (since the thickness of the GO film is ~220 nm), while some of the energetic electrons are back-scattered from the primary collision. The more energetic the electron, the further it will penetrate into substrate and make it harder to go back into the sample. Hence there will be less BSEs that could possibly return to the sample and cause deoxygenation. In the back-scattering process, the BSEs travel through the material and substrate in somewhat random

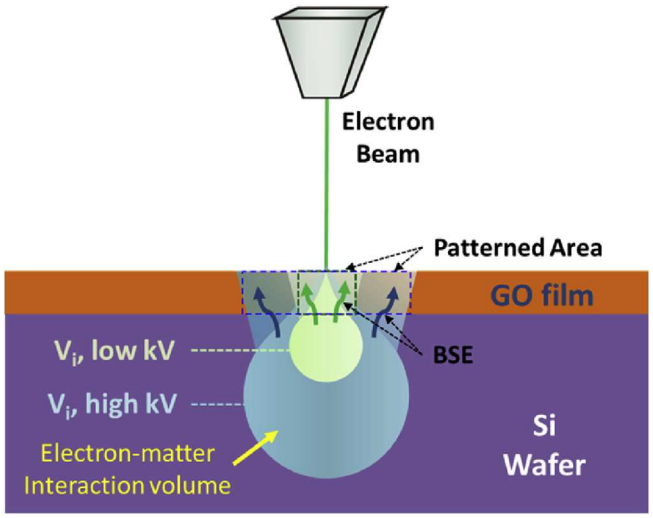

Fig. 7. A schematic diagram illustrating the electron–matter interaction volume and the expected patterning area on GO at low (green) and high (blue) beam accelerating voltages. (A colour version of this figure can be viewed online.)

directions, and generate secondary electrons along the trajectory through inelastic collisions. In a consequence, the surface distribution radius of BSEs could closely resemble the extended length of the pattern. Overall, the reductive e-beam deoxygenation of GO is more effective by using low-energy e-beam and the patterning result is very predictable with the classical theory of electron–matter interaction with the help of the Monte Carlo simulation.

4. Conclusion

Low-energy electron-beam was demonstrated as an efficient technique in writing deoxygenated micro-patterns on a GO film. The pattern features were carefully characterized with several microscopy and spectroscopy methods. Our results show that e-beam can effectively deoxygenate a GO film, leading to film shrinkage without distorting the original lattice configuration. The degree of deoxygenation increases with the electron doses, while the patterning efficiency and lithographic resolution are inversely proportional to the applied beam voltage. The observed phenomena were further justified by Monte Carlo simulations of projected electron trajectories. This work can guide use of EBL technology on graphene-based materials for all-carbon electronics.

Acknowledgment

The authors acknowledge the financial support from the University of Queensland (ECR009132 and NSRSU600211), the University of New South Wales, and support of the Centre for Microscopy and Microanalysis at the University of Queensland through their facilities, and the scientific and technical assistance. This work was performed in part at the Qld node of the Australian National Fabrication Facility, a company established under the National Collaborative Research Infrastructure Strategy to provide nano and micro-fabrication facilities for Australia's researchers. Special assistance from Dr Barry Wood and Mr Ron Rash for the XPS and EDS measurements is also gratefully acknowledged.

Appendix A. Supporting information

Supporting information related to this article can be found at http://dx.doi.org/10.1016/j.carbon.2015.08.116.

References

[1] K.S. Novoselov, A.K. Geim, S.V. Morozov, D. Jiang, Y. Zhang, S.V. Dubonos, et al., Electric field effect in atomically thin carbon films, Science 306 (5696) (2004) 666–669.

[2] A.K. Geim, K.S. Novoselov, The rise of graphene, Nat. Mater. 6 (3) (2007) 183–191.

[3] Y. Zhou, K.P. Loh, Making patterns on graphene, Adv. Mater. 22 (32) (2010) 3615–3620.

[4] M.Y. Han, B. Özyilmaz, Y. Zhang, P. Kim, Energy band-gap engineering of graphene nanoribbons, Phys. Rev. Lett. 98 (20) (2007) 206805.

[5] K. Nakada, M. Fujita, G. Dresselhaus, M.S. Dresselhaus, Edge state in graphene ribbons: nanometer size effect and edge shape dependence, Phys. Rev. B 54 (24) (1996) 17954–17961.

[6] F. Cervantes-Sodi, G. Csányi, S. Piscanec, A.C. Ferrari, Edge-functionalized and substitutionally doped graphene nanoribbons: electronic and spin properties, Phys. Rev. B 77 (16) (2008) 165427.

[7] X. Li, X. Wang, L. Zhang, S. Lee, H. Dai, Chemically derived, ultrasmooth graphene nanoribbon semiconductors, Science 319 (5867) (2008) 1229–1232.

[8] H. Seo, S. Ahn, J. Kim, Y.-A. Lee, K.-H. Chung, K.-J. Jeon, Multi-resistive reduced graphene oxide diode with reversible surface electrochemical reaction induced carrier control, Sci. Rep. 4 (2014).

[9] S. Wang, P.K. Ang, Z. Wang, A.L.L. Tang, J.T.L. Thong, K.P. Loh, High mobility, printable, and solution-processed graphene electronics, Nano Lett. 10 (1) (2010) 92–98.

[10] W. Gao, N. Singh, L. Song, Z. Liu, A.L.M. Reddy, L.J. Ci, et al., Direct laser writing of micro-supercapacitors on hydrated graphite oxide films, Nat. Nanotechnol. 6 (8) (2011) 496–500.

[11] M.F. El-Kady, V. Strong, S. Dubin, R.B. Kaner, Laser scribing of high-performance and flexible graphene-based electrochemical capacitors, Science 335 (6074) (2012) 1326–1330.

[12] F. Torrisi, T. Hasan, W. Wu, Z. Sun, A. Lombardo, T.S. Kulmala, et al., Inkjet-printed graphene electronics, ACS Nano 6 (4) (2012) 2992–3006.

[13] L. Huang, Y. Huang, J. Liang, X. Wan, Y. Chen, Graphene-based conducting inks for direct inkjet printing of flexible conductive patterns and their applications in electric circuits and chemical sensors, Nano Res. 4 (7) (2011) 675–684.

[14] B. Standley, A. Mendez, E. Schmidgall, M. Bockrath, Graphene–graphite oxide field-effect transistors, Nano Lett. 12 (3) (2012) 1165–1169.

[15] Y. Chen, Y. Xu, K. Zhao, X. Wan, J. Deng, W. Yan, Towards flexible all-carbon electronics: flexible organic field-effect transistors and inverter circuits using solution-processed all-graphene source/drain/gate electrodes, Nano Res. 3 (10) (2010) 714–721.

[16] J. Liang, Y. Chen, Y. Xu, Z. Liu, L. Zhang, X. Zhao, et al., Toward all-carbon electronics: fabrication of graphene-based flexible electronic circuits and memory cards using maskless laser direct writing, ACS Appl. Mater. Interfaces 2 (11) (2010) 3310–3317.

[17] B. Li, X. Cao, H.G. Ong, J.W. Cheah, X. Zhou, Z. Yin, et al., All-carbon electronic devices fabricated by directly grown single-walled carbon nanotubes on reduced graphene oxide electrodes, Adv. Mater. 22 (28) (2010) 3058–3061.

[18] E. Shi, H. Li, L. Yang, J. Hou, Y. Li, L. Li, et al., Carbon nanotube network embroidered graphene films for monolithic all-carbon electronics, Adv. Mater. 27 (4) (2015) 682–688.

[19] G. Eda, M. Chhowalla, Chemically derived graphene oxide: towards large-area thin-film electronics and optoelectronics, Adv. Mater. 22 (22) (2010) 2392–2415.

[20] G. Eda, C. Mattevi, H. Yamaguchi, H. Kim, M. Chhowalla, Insulator to semimetal transition in graphene oxide, J. Phys. Chem. C 113 (35) (2009) 15768–15771.

[21] Z. Luo, Photoluminescence and band gap modulation in graphene oxide, Appl. Phys. Lett. 94 (11) (2009) 111909.

[22] J. Meihua, J. Hae-Kyung, Y. Woo Jong, B. Dong Jae, K. Bo Ram, L. Young Hee, Graphene oxide thin film field effect transistors without reduction, J. Phys. D. Appl. Phys. 42 (13) (2009) 135109.

[23] H.K. Jeong, M.H. Jin, K.P. So, S.C. Lim, Y.H. Lee, Tailoring the characteristics of graphite oxides by different oxidation times, J. Phys. D. Appl. Phys. 42 (6) (2009) 065418.

[24] Y.-W. Lan, W.-H. Chang, B.-T. Xiao, B.-W. Liang, J.-H. Chen, Jiang P-h, et al., Polymer-free patterning of graphene at sub-10-nm scale by low-energy repetitive electron beam, Small 10 (22) (2014) 4778–4784.

[25] L. Chen, Z. Xu, J. Li, C. Min, L. Liu, X. Song, et al., Reduction and disorder in graphene oxide induced by electron-beam irradiation, Mater. Lett. 65 (8) (2011) 1229–1230.

[26] P. Kumar, K.S. Subrahmanyam, C.N.R. Rao, Graphene patterning and lithography employing laser/electron-beam reduced graphene oxide and hydrogenated graphene, Mater. Exp. 1 (3) (2011) 252–256.

[27] S. Kim, D.D. Kulkarni, M. Henry, P. Zackowski, S.S. Jang, V.V. Tsukruk, et al., Localized conductive patterning via focused electron beam reduction of graphene oxide, Appl. Phys. Lett. 106 (13) (2015) 133109.

[28] P.A. Peterson, Z.J. Radzimski, S.A. Schwalm, P.E. Russell, Low-voltage electron beam lithography, J. Vac. Sci. Technol. 10 (6) (1992) 3088–3093.

[29] C.K. Harnett, K.M. Satyalakshmi, H.G. Craighead, Low-energy electron-beam patterning of amine-functionalized self-assembled monolayers, Appl. Phys. Lett. 76 (17) (2000) 2466–2468.

[30] D.M. Tanenbaum, C.W. Lo, M. Isaacson, H.G. Craighead, M.J. Rooks, K.Y. Lee, et al., High resolution electron beam lithography using ZEP-520 and KRS resists at low voltage, J. Vac. Sci. Technol. 14 (6) (1996) 3829–3833.

[31] K.-H. Wu, D.-W. Wang, I.R. Gentle, The value of mixed conduction for oxygen electroreduction on graphene–chitosan composites, Carbon 73 (0) (2014) 234–243.

[32] Z.Q. Wei, D.B. Wang, S. Kim, S.Y. Kim, Y.K. Hu, M.K. Yakes, et al., Nanoscale tunable reduction of graphene oxide for graphene electronics, Science 328 (5984) (2010) 1373–1376.

[33] D.C. Marcano, D.V. Kosynkin, J.M. Berlin, A. Sinitskii, Z.Z. Sun, A. Slesarev, et al., Improved synthesis of graphene oxide, ACS Nano 4 (8) (2010) 4806–4814.

[34] A. Bagri, C. Mattevi, M. Acik, Y.J. Chabal, M. Chhowalla, V.B. Shenoy, Structural evolution during the reduction of chemically derived graphene oxide, Nat. Chem. 2 (7) (2010) 581–587.

[35] A. Ganguly, S. Sharma, P. Papakonstantinou, J. Hamilton, Probing the thermal deoxygenation of graphene oxide using high-resolution in situ X-ray-based spectroscopies, J. Phys. Chem. C 115 (34) (2011) 17009–17019.

[36] A.C. Ferrari, J.C. Meyer, V. Scardaci, C. Casiraghi, M. Lazzeri, F. Mauri, et al., Raman spectrum of graphene and graphene layers, Phys. Rev. Lett. 97 (18) (2006) 187401.

[37] J. Shang, L. Ma, J. Li, W. Ai, T. Yu, G.G. Gurzadyan, The origin of fluorescence from graphene oxide, Sci. Rep. 2 (2012).

[38] D. Drouin, A.R. Couture, D. Joly, X. Tastet, V. Aimez, R. Gauvin, CASINO V2.42—a fast and easy-to-use modeling tool for scanning electron microscopy and microanalysis users, Scanning 29 (3) (2007) 92–101.